Available online at www.sciencedirect.com

ScienceDirect

Ceramics International 40 (2014) 4663–4671

CERAMICS INTERNATIONAL

www.elsevier.com/locate/ceramint

Microstructure characterization of thermal barrier coating systems after controlled exposure to a high temperature

Julián D. Osorio[a,b,*], Juan P. Hernández-Ortiz[a,c], Alejandro Toro[d]

[a]Materials and Minerals Department, National University of Colombia, Medellín, Colombia
[b]Department of Mechanical Engineering, Florida State University, Tallahassee, Fl, 32306, USA
[c]BioTechnology Center, Genomics Center of Wisconsin, University of Wisconsin-Madison, WI, 53706, USA
[d]Tribology and Surfaces Group, National University of Colombia, Medellín, Colombia

Received 27 April 2013; received in revised form 22 July 2013; accepted 2 September 2013
Available online 7 September 2013

Abstract

Air plasma spray-deposited thermal barrier coatings were thoroughly characterized after exposure to a high temperature. Microstructural changes in the thermal barrier coatings, as a function of temperature and soaking time, are reported. Pores in the ceramic top coat were redistributed and rounded due to sintering, which increases density and thermal conductivity. Formation of the undesirable monoclinic phase was detected after 600 h at 1100 °C; the amount of this phase increased with exposure time, reaching 18 wt% after 1000 h. The thermally grown oxide layer reached a critical thickness of 5 μm after 600 h at 1100 °C even though no delamination was observed after 1700 h of exposure when the thickness was around 6.7 μm. Ni- and Cr-enriched oxides were formed, which, in theory, should favor crack generation and propagation. After 1000 h, a large amount of precipitates in the Ni-base substrate were observed and characterized.

Keywords: TBC; Characterization; High temperature; Phase transformation

1. Introduction

Thermal barrier coatings (TBCs) have been developed to protect critical-path components in gas turbines against erosion and corrosion at high temperatures [1–5]. They provide thermal insulation of the metallic substrates in addition to increasing operational temperatures and the efficiency of power generation plants and aircraft engines [4–7]. A conventional TBC system consists of three layers which are applied onto a substrate or base metal (BM): the thermal coating or top coat (TC), the bond coat (BC) and the thermally grown oxide (TGO). Fig. 1 shows a SEM cross-sectional view of a TBC system applied by an air plasma splay (APS) technique.

The top coat (TC) is constituted by zirconium dioxide or zirconia (ZrO_2), which exhibits a tetragonal phase at high temperatures (above 1000 °C). Tetragonal ZrO_2 is stabilized by the addition of yttrium (Y) or other species, such as hafnium (Hf) [8–11]. If no stabilizer is added, the tetragonal phase transforms to a monoclinic phase during cooling. This transformation is undesirable because the monoclinic phase has lower mechanical properties than the tetragonal phase. In addition, there is a significant volume change (around 5%) that causes cracking and failure [3,12,13]. The TC is deposited onto a metallic layer, the bond coat (BC), through either air plasma spray (APS) or electron beam-physical vapor deposition (EB-PVD) processes. The TC has high porosity that reduces thermal conductivity and allows combustion gases to diffuse within the layer [1,14–16]. There are two major types of bond coats (BCs): platinum-modified nickel aluminide (PtNiAl) and MCrAlY alloy (where M refers to one or more of the elements Co, Ni and Fe). In the initial stages of the TBC system, the BC provides adherence between the TC and the substrate. The BC also gives oxidation protection to the substrate [17–19]. It contains a considerable amount of aluminum in order to serve as a reservoir for this element towards the formation of the thermally grown oxide (TGO) layer at the TC/BC interface. Particularly, the MCrAlY bond coat type contains 7–10 wt% Al. Once the TGO is formed, the BC provides the anchoring between the TGO and the substrate.

*Corresponding author. Tel.: + 18505705716.
E-mail addresses: jdosorio@unal.edu.co, jdo12@fsu.edu (J.D. Osorio).

0272-8842/$ - see front matter © 2013 Elsevier Ltd and Techna Group S.r.l. All rights reserved.
http://dx.doi.org/10.1016/j.ceramint.2013.09.007

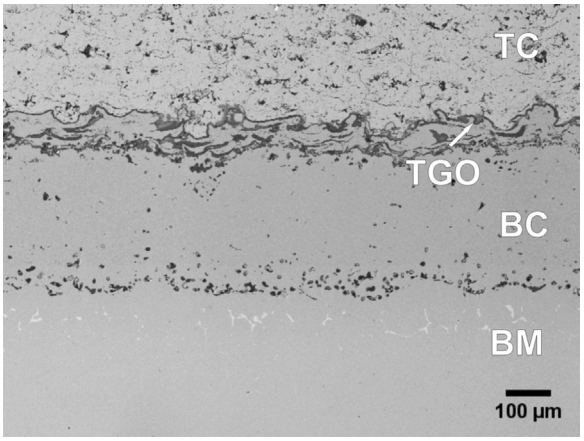

Fig. 1. Cross-sectional view of a TBC system deposited by APS process. Four layers can be observed: base metal (BM), bond coat (BC), thermally grown oxide (TGO) and top coat (TC), SEM.

The TGO is a ceramic layer which grows as a consequence of aluminum and oxygen diffusion through the BC and the TC, respectively. The TBCs are designed so α-Al_2O_3 based layers form and grow slowly, becoming a barrier to oxygen diffusion towards the substrate, further avoiding oxidation of the substrate. However, the growth of this layer can generate stresses which, in combination with the BC/TC interfacial imperfections, are responsible for many of the TBC failure mechanisms [20–24]. It has been reported that TBC failure occurs when the TGO layer is around 6 μm thick [25–27]. Formation of α-Al_2O_3 is desirable because it provides strong TC/BC adherence and it exhibits a slower growth rate than other oxides [28,29]. Many components exposed to high temperatures in gas turbines are manufactured using Ni-based superalloy substrates, which offer good mechanical strength and excellent corrosion, oxidation and erosion resistances at high temperatures [30,31]. These superalloys can contain significant amounts of alloying elements such as Cr, Mo, Al, Ti, Fe and C [32,33] and their microstructure is composed of highly stable austenite [32]. The addition of aluminum and titanium promotes the formation of intermetallic compounds such as Ni_3Al, Ni_3Ti and $Ni_3(Al, Ti)$ while Cr, Mo and C favor M_6C, $M_{23}C_6$ and M_7C_3-type carbide precipitation [33,34]. These precipitates improve creep resistance of the superalloy due to their grain boundary pinning action [32].

The fast technological developments and rising demand of energy resources require manufacturing new materials to increase gas turbines' efficiency and extend their lifetime. To succeed in this enterprise, a detailed knowledge of the current materials used in gas turbines' manufacturing is required. In this paper, Scanning Electron Microscopy (SEM), X-ray Diffraction (XRD), Transmission Electron Microscopy (TEM), Energy-Dispersive X-ray Spectroscopy (EDXS) and Wavelength-Dispersive X-ray Spectrometry (WDXS) were used to characterize the layers of an APS-applied TBC system. Changes of some important features of all the layers in the TBC were studied as a function of high temperature exposure and correlated with failure mechanisms of TBC systems. The results are believed to be useful in contributing to the current discussion in controversial fields such as the phase stability in the TC, the kinetics of TGO formation and the microstructural response of the substrate to high temperature exposition. The paper is organized as follows: Section 2 explains the experimental procedure, the methods and the materials. In Section 3, the results, for each component of a TBC system, are presented. Lastly, the most important findings are summarized in Section 4.

2. Materials and methods

The TBC system studied consisted of an Inconel 625 substrate with MCrAlY bond coat applied by High Velocity Oxygen Fuel (HVOF) process and APS-deposited ZrO_2-6–8 wt% Y_2O_3 top coat as shown in Fig. 1. The TC feedstock consisted in vacuum-atomized spherical particles with an average diameter of ~60 μm (minimum size 45 μm—maximum size 90 μm), containing about 68.8 wt% Zr, 31.4 wt% O, 5.8 wt% Y and traces of Hf that could not be detected by EDXS microanalysis. On the other hand, the BC powders were vacuum-atomized spherical particles with an average diameter of 45 μm (minimum size 10 μm—maximum size 60 μm), which were mainly composed of Ni (48.4 wt%), Co (23.1 wt %), Cr (21.9 wt%), Al (5.5 wt%) and O (1.2 wt%). Prior to deposition the metallic substrate was sand blasted in order to obtain a surface with Ra between 3 and 6 μm. HVOF bond coat deposition was done with oxygen flow rate of 4 $m^3\ s^{-1}$, propylene flow rate of 1 $m^3\ s^{-1}$ and the stand-off distance was 0.4 m with horizontal spray jet. On the other hand, the top coat was applied by using a d.c. plasma torch with anode-nozzle internal diameter of 8 mm, plasma current of 600 A, plasma voltage of 70 V, injection angle of 90°, stand-off distance of 0.9 m and a flow rate of 8.3 $m^3\ s^{-1}$ Ar and 2.5 $m^3\ s^{-1}$ H_2.

The specimens were cut from a $30 \times 30\ cm^2$ plate using a precision saw cutting machine operating at 4000 rpm and 1.2 mm/min feed-rate; then, eight samples were treated at 1100 °C in a normal atmosphere with exposure times of 1, 100, 200, 400, 600, 800, 1000 and 1700 h respectively. Then, they were cooled in air. To ensure the reliability of the results, a replica for each heat treatment condition was also performed. The heating rate for the treatments was 18 °C/min. Despite the fact that the exposure temperature of 1100 °C can be too high for the Inconel 625, no evidence of damage by TC delamination was observed after the heat treatments in any sample. The samples for microscopic examination were prepared following the polishing sequence described in Table 1.

SEM examination included EDXS and WDXS microanalysis for samples exposed at different high-temperature conditions. WDXS was performed in order to obtain a quantitative measurement of the elements present in small concentrations of the sample. For all measurements, an adequate Interaction Volume (I.V.) was verified using the Kanaya–Okayama expression [35]. The volumetric porosity percentage (P^*) in the TC was determined through Image Analysis technique (IA) with the aid of the Otsu criteria for thresholding [36]. EDXS compositional maps were obtained to identify the elements present in the precipitates of the Inconel 625 substrate. The phases present in the TC were analyzed using an X-Ray diffractometer with a

Table 1
Polishing sequence for microscopic examination.

	Cloth	Time (min)	Abrasive
1	–	5	Emery paper no. 400
2	–	5	Emery paper no. 600
3	Ultrapath	10	Diamond suspension 12 μm
4	Texmet	15	Diamond suspension 6 μm
5	Texmet	15	Diamond suspension 3 μm
6	Microcloth	60	Diamond suspension 1 μm

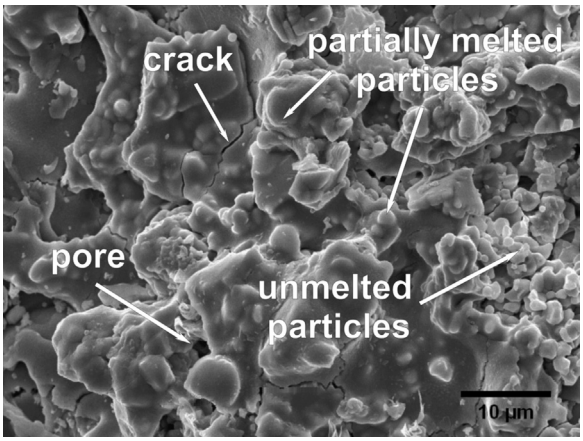

Fig. 2. SEM top view of a TC treated at 1100 °C—1700 h.

CuKα radiation gun. The Rietveld semiquantitative refinement was performed to determine the content of the monoclinic phase as a function of the exposure time at 1100 °C.

3. Results and discussion

3.1. Ceramic top coat

A SEM top view of the TC after heat treatment at 1100 °C during 1700 h is shown in Fig. 2. The cauliflower-like microstructure observed is characteristic of the APS-deposited layers. A considerable amount of unmelted and partially melted ceramic particles can be observed. This microstructural feature is relevant because these particles can detach and be dragged by the combustion gasses during operational components of the gas turbine. Therefore, a solid impingement erosion mechanism is constituted, accelerating degradation of the system [20].

Fig. 3a shows a cross-sectional view of the TC in the as-sprayed condition, in which a large amount of open pores and splats can be seen. Fig. 3b–d presents cross-sectional views of the TC after exposure to 1100 °C for different time. Additional features of APS-deposited TC microstructures are recognized, such as the presence of splats and a considerable amount of pores and cracks. Pores are generally aligned perpendicularly to the heat flux (see Fig. 3b and c) and they lie along the splats' longest dimension. These pores and cracks can be also identified in Fig. 2. Pores play a role as stress concentrators, promoting cracking and subsequent fracture [37]. Nonetheless, porosity in the TC could be beneficial because it reduces the heat conduction to the substrate [1,15]. At high operating temperatures, diffusion-controlled sintering is activated [38–40], resulting in a denser ceramic that increases strength while reducing the insulating capacity. In the as-sprayed condition sample (Fig. 3a), numerous pores with sharp edges and open cracks were observed; features that changed when the samples were exposed to a high temperature (Fig. 3b–d). When the exposure time reached 1700 h the pores were much smaller and rounded, as expected for a closed porosity condition. The image analysis indicated an initial volumetric porosity (P^*) of 6.86% ± 0.85% for the as-sprayed condition; this volumetric porosity reduced to 4.75% ± 0.65% after 1700 h at 1100 °C, which is consistent with microstructure evolution as shown in Fig. 3.

EDXS and WDXS chemical microanalyses for the TC were performed in order to verify the Zr/O stoichiometric relation for ZrO_2 and to provide a quantitative measurement of the stabilizer concentration. The EDXS analysis yielded 36.2 at% (76.4 wt%) Zr, and 63.8 at% (23.6 wt%) O, which is close to the 1:2 atomic stoichiometric ratio. The WDXS measurements showed that yttrium (3.17 ± 0.20 wt%) and hafnium (1.14 ± 0.03 wt%) were added to stabilize the tetragonal phase of ZrO_2. As expected, the chemical composition of the TC in the as-sprayed condition presented a slight variation when compared to that of the powder feedstock as a consequence of air oxidation and surface chemical reactions during the application process.

Yttrium and hafnium are among the elements that stabilize the tetragonal phase at room temperature [11,25,41]. These elements help the TC to reduce its thermal conductivity by changing the crystal structure of the material in such a way that an un-harmonic scattering of charge carriers occurs. At high temperatures, the charge carriers responsible for heat conduction within the ceramic crystals are the phonons [8,23]. Un-harmonic phonon scatter to reduce thermal conductivity is accomplished through the addition of yttrium ions (Y^{+3}) and hafnium ions (Hf^{+4}) which replace zirconium ions (Zr^{+4}) in the crystal lattice. The main effect of adding Y^{+3} ions is to produce oxygen vacancies. On the other hand, even though Hf^{+4} ions are chemically similar and have comparable ionic radius to Zr^{+4} ions, they are almost twice as massive, generating a lattice disorder [8,23,25].

The initial microstructure of the TC in this study consisted of a mixture of tetragonal and cubic phases. It has been well established in the literature that this mixture is stable between room and service temperatures if the amount of Y_2O_3 (yttria) is 6–8 wt% [25,42]. A different amount of yttria can cause a monoclinic phase transformation, which is associated with a 4–5% volume expansion [42,43]. In the as-sprayed condition, the Rietveld refinement of XRD data showed that the TC is composed of 93 wt% tetragonal phase and 7 wt% cubic phase (no monoclinic phase was detected). To determine the yttria concentration in the tetragonal phase based on the change in lattice parameters, the following equation was used [44,45]:

$$YO_{1.5}\ (\text{mol}\%) = \frac{1.0225 - c/a}{0.001311}, \qquad (1')$$

where a and c are the lattice parameters of the tetragonal phase in angstroms.

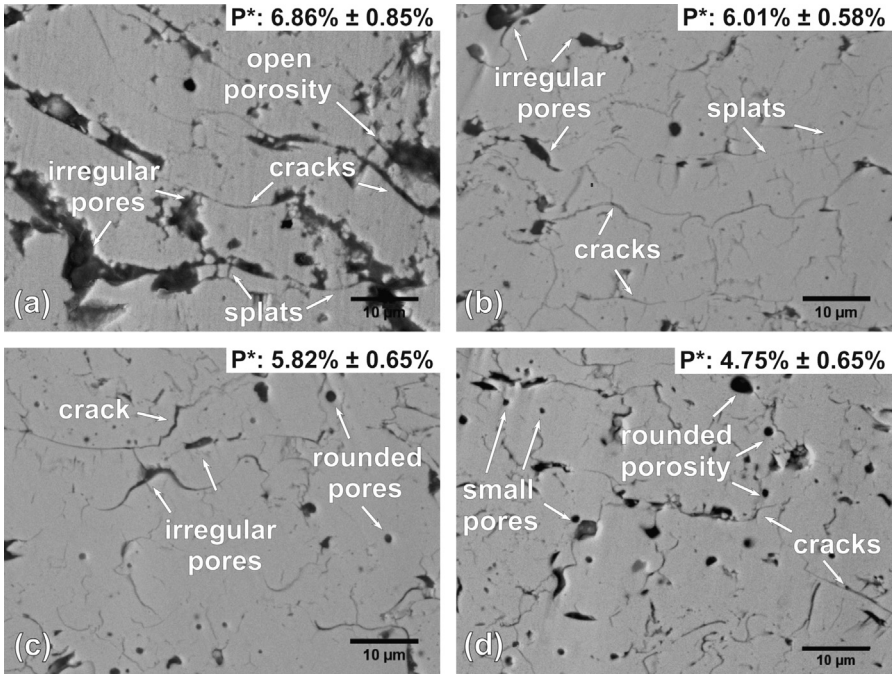

Fig. 3. TC cross-sectional views of the TC: (a) as-sprayed condition and exposed to 1100 °C for different time: (b) 400 h; (c) 800 h and (d) 1700 h. In each case, the average of 10 measurements of volumetric porosity percentage (P^*) is shown.

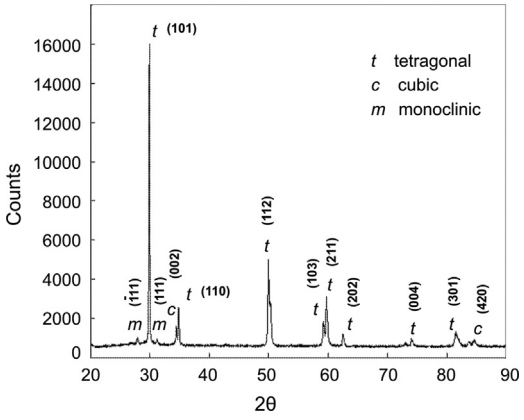

Fig. 4. X-Ray diffractogram of TC sample treated during 1700 h at 1100 °C.

According to Eq. (1), the concentration of $YO_{1.5}$ in the tetragonal phase was 7.85 mol% (~7.85 wt% Y_2O_3). This amount is within the recommended range to stabilize the tetragonal phase at high temperatures (6–8 wt% Y_2O_3) [4,25].

An X-Ray diffractogram of the TC is shown in Fig. 4 for a sample treated at 1100 °C during 1700 h. The material was essentially a mixture of tetragonal and cubic phases, with a small amount of a monoclinic phase. This monoclinic phase formed after 600 h and its mass fraction, which was calculated through Rietveld analysis, increased with treatment time as shown in Fig. 5. The monoclinic phase content increased from 1.8 wt% for exposure time of 800 h to 23.4 wt% after 1700 h. The tetragonal to monoclinic transformation occurs because prolonged exposure to high temperatures favors the yttrium diffusion to the cubic phase from the tetragonal phase, eventually transforming to a monoclinic phase during cooling. As a consequence, the yttrium concentration in the tetragonal phase decreases and monoclinic phase becomes more stable. It is important to point out, however, that the amount of monoclinic phase present in the microstructure not only depends on the yttrium concentration, but also on the powder feedstock morphology and grain size, among other factors [46].

3.2. Bond coat

As shown in Fig. 1, the BC consists of a dense metallic layer with a thin porous film and disperse oxide deposits next to the TGO/TC interface, which are typical features of the microstructure of HVOF-applied coatings. Fig. 6 shows a SEM micrograph of the bond coat. This layer was analyzed through EDXS and the results are summarized in Table 2. The results indicated that chemical composition corresponded to the NiCoCrAlY BC type. The BC microstructure was a mixture of two phases, as shown in Fig. 6: Co–Ni–Cr enriched γ (brighter zones) and Ni–Al enriched β (darker zones). Higher Cr contents make the BC able to resist oxidation and corrosion. Other typical BCs, such as the NiCoAlY and NiCrAlY type, present higher oxidation resistance but lower corrosion resistance [32]. A small amount of yttrium was found in the BC (see Table 2). This element is added in order to enhance the TGO's adherence to the BC because it prevents segregation of sulfur to the TGO layer [19].

3.3. Thermally grown oxide

Many of the failure mechanisms in TBCs are related to the formation and growth of the TGO [24,29,47–49]. The stresses developed during the growth of this layer promote crack

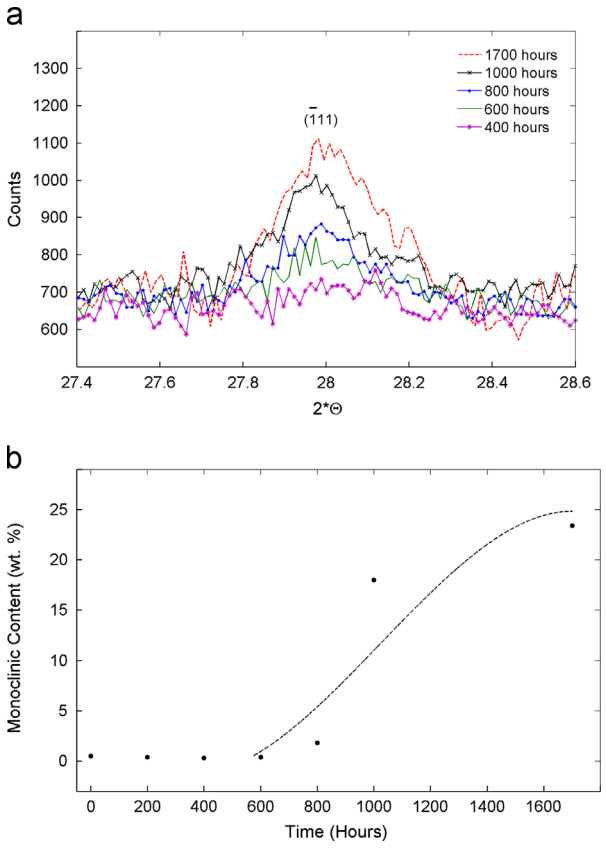

Fig. 5. (a) X-Ray diffractograms of TC sample treated at 1100 °C as a function of the exposure time. The peak corresponding to monoclinic phase appears after 600 h of treatment. (b) Monoclinic phase content in APS-deposited TC as a function of exposure time to 1100 °C, calculated through the Rietveld refinement.

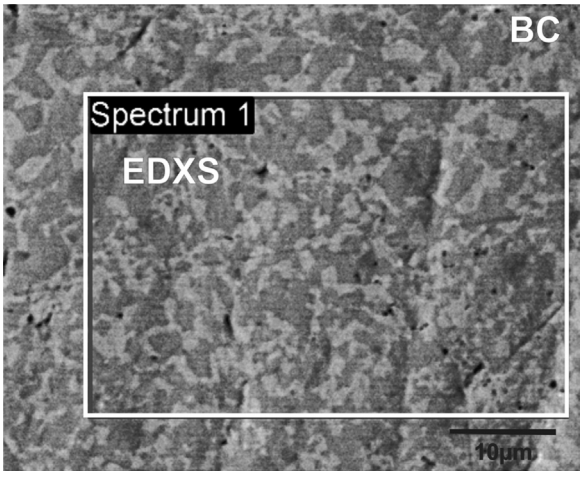

Fig. 6. Micrograph of the BC. Two phases can be distinguished: Co–Ni–Cr enriched γ (brighter zones) and Ni–Al enriched β (darker zones), SEM.

initiation and propagation within the layer itself and at the TGO/TC and BC/TGO interfaces [20–22,47,48]. These cracks can cause delamination of the TC and subsequent loss of the protection against corrosion and erosion at high temperatures. SEM micrographs of samples treated at 1100 °C during 10, 400, 800 and 1700 h respectively, are shown in Fig. 7. The

Table 2
Bond coat and TGO chemical microanalysis.

	BC	TGO	
	EDXS, wt%	EDXS-1, wt%	EDXS-2, wt%
Ni	53.6	–	31.8
Co	21.6	–	–
Cr	14.9	–	21.4
Al	8.8	54.3	19.0
O	–	43.5	25.8
Y	0.5	2.1	2.1

images clearly show the direct relation between the thickness of the TGO and exposure time to high temperatures. In Fig. 8, the TGO growth as a function of exposure time at 1100 °C is shown; it can be seen that the thickness of the TGO presented a power law dependence with time with an exponent of 1/2, which is in agreement with the theoretical diffusion control mechanism. Although the TGO reached a thickness of 6.7 μm after 1700 h at 1100 °C, no delamination evidences were detected. The TGO growth also generates compressive stresses that cause distortions in the system, leading to an undulated shape at the TGO/TC interface [22,47,50]. This undulation, which is often called "ratcheting," is commonly observed when the TBC is subjected to thermal cycling [50–52].

Generally speaking, it is desirable that the TGO grows only as Al_2O_3 due to its superior protective properties. However, other oxides, such as $(Cr, Al)_2O_3$, $Ni(Cr, Al)_2O_4$ and NiO, can be formed after 800 h exposure at 1100 °C, as shown in Figs. 7c and d, and 9, and Table 2. Chemical microanalyses performed by EDXS in two specific regions of the TGO layer revealed that, besides Al_2O_3 (EDXS-1 in Fig. 9, darker area) a Ni, Cr-enriched oxide was formed (EDXS-2 in Fig. 9, brighter area). This complex oxide is porous and can grow towards the BC or the TC. In the first case (towards the BC), the Ni, Cr-enriched oxides formed in the BC during the initial stages of the TBC's lifetime, i.e. when alumina has not formed yet. This can be attributed, according to the phase diagram shown in Fig. 10, to the compositional inhomogeneity of the bond coat in such a way that regions with lower aluminum concentration help oxides such as $(Cr, Al)_2O_3$ and eventually NiO become more stable than Al_2O_3 [53,54]. In the second case (towards the TC), the oxides in the TC are the result of the diffusion of Ni, Cr and Al through the TGO during the TBC exposure at high temperatures [55].

For longer exposure times, it is possible that $(Cr, Al)_2O_3$, Ni $(Cr, Al)_2O_4$ and NiO form from the existing TGO layer through the chemical reactions, i.e. [23]

$$Al_2O_3 + 2Cr \rightarrow Cr_2O_3 + 2Al, \quad (1)$$

$$Al_2O_3 + \tfrac{1}{2}O_2 + Ni \rightarrow NiAl_2O_4. \quad (2)$$

The formation of these oxides is detrimental to TBC durability because they promote nucleation and propagation of cracks, present lower adhesion properties and allow rapid diffusion of oxygen towards the substrate [51,53,55].

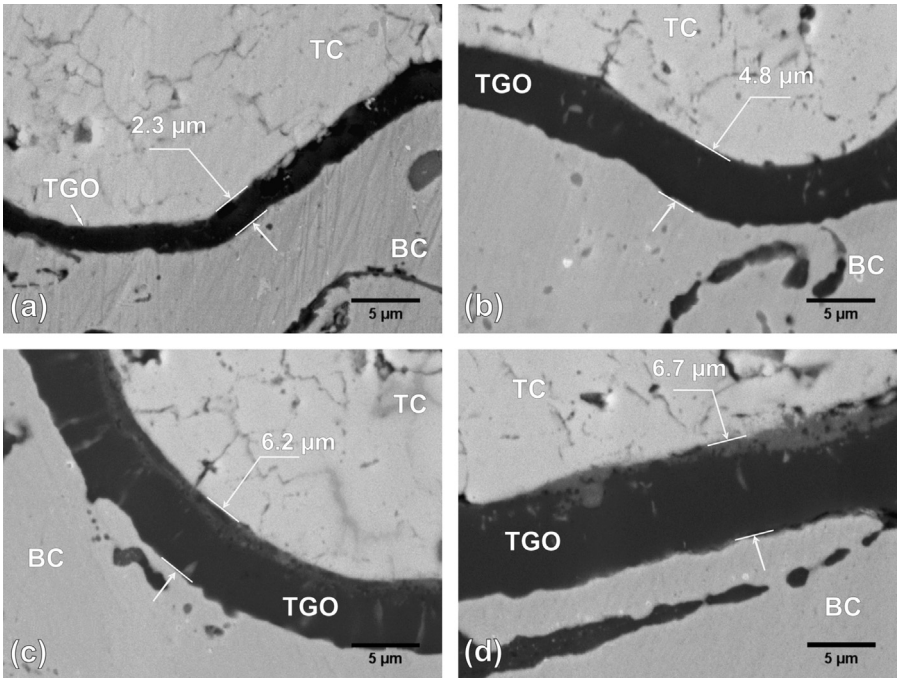

Fig. 7. Variation of thickness of TGO with exposure time at 1100 °C. (a) 10 h, (b) 400 h (c) 800 h and (d) 1700 h. SEM.

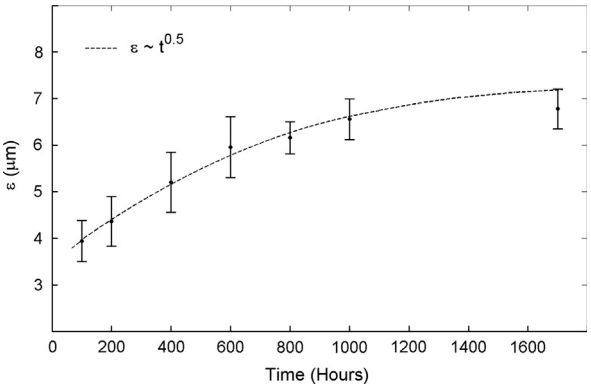

Fig. 8. Experimental TGO growth in TBC samples treated at 1100 °C with exposures times from 100 to 1700 h.

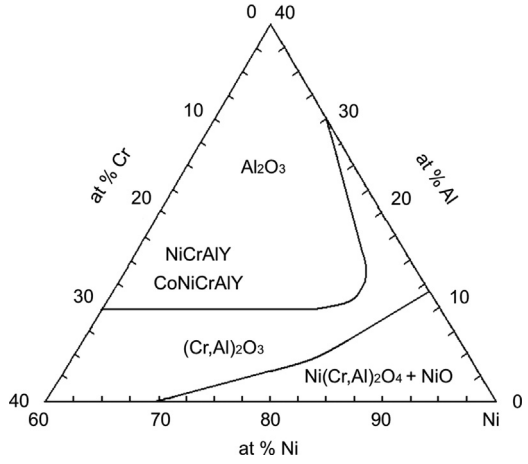

Fig. 10. Ternary phase diagram for Al, Cr and Ni [53,54].

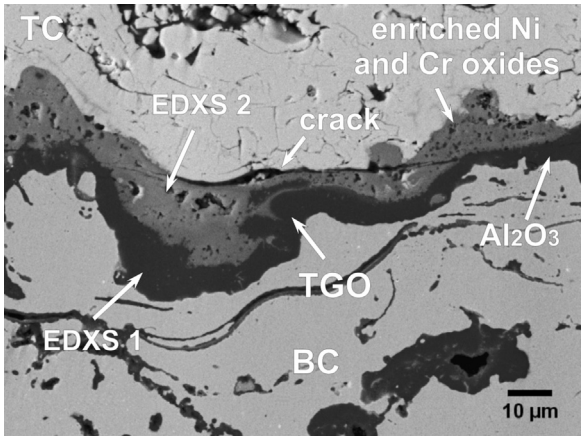

Fig. 9. TGO micrograph containing Ni–Cr oxide, the sample was treated at 1100 °C during 1000 h, SEM.

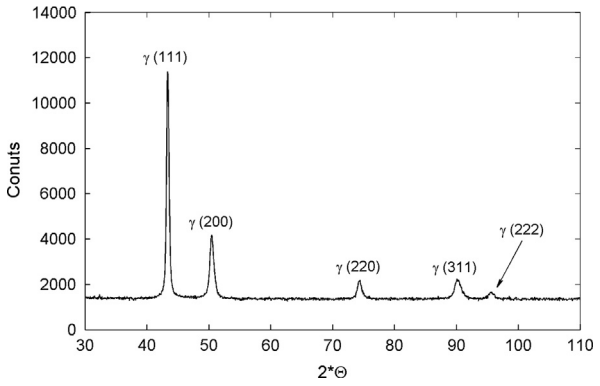

Fig. 11. X-Ray diffractogram of the substrate sample treated during 100 h at 1100 °C.

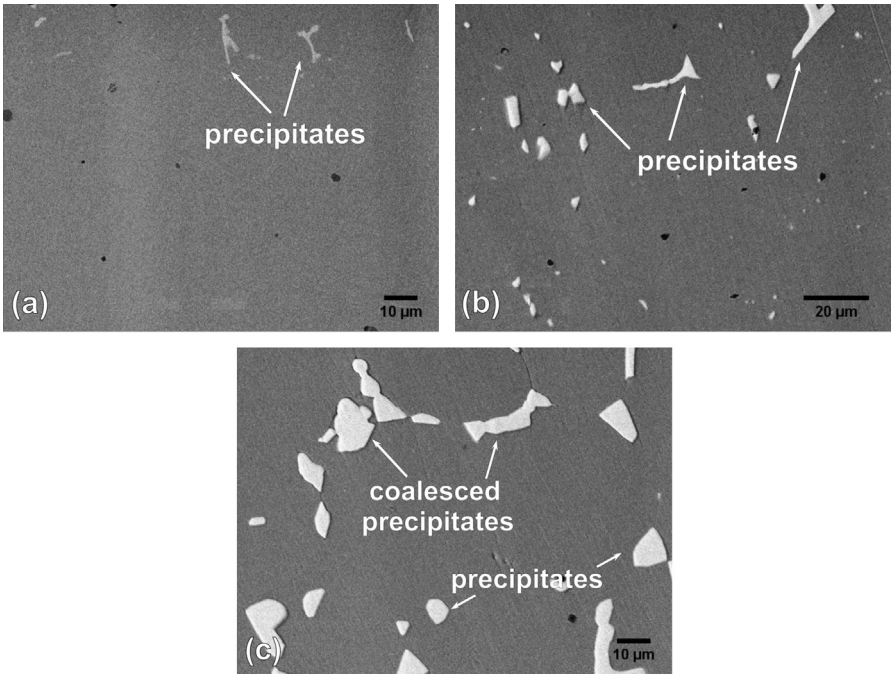

Fig. 12. Microstructures of Inconel 625 substrate: (a) untreated sample, (b) sample treated at 1100 °C for 100 h and (c) sample treated at 1100 °C for 1000 h, SEM.

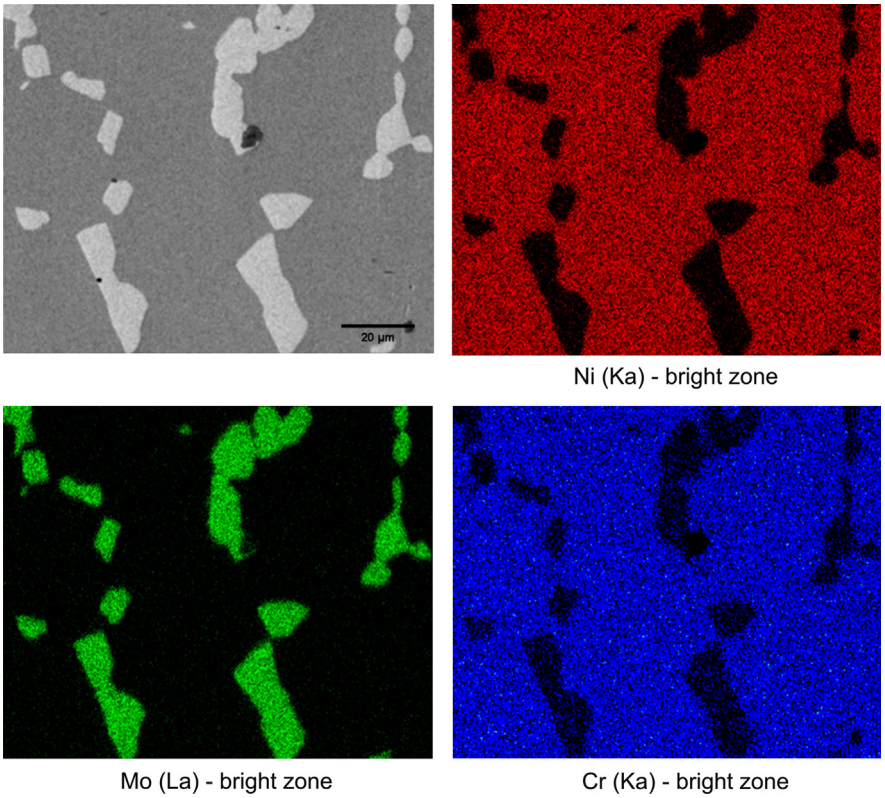

Fig. 13. EDXS compositional maps for Inconel 625 substrate heat treated at 1100 °C during 1000 h.

3.4. Substrate

An X-Ray diffractogram of the substrate after 100 h exposure to 1100 °C is shown in Fig. 11, in which, clearly, austenite is the only phase found in the microstructure. Although no precipitates were detected in this diffractogram because of their low volumetric fraction, they were readily observed after microscopic examination of polished samples as shown in Fig. 12. Fig. 12a shows a reference sample not exposed to a high temperature, where small and disperse precipitates can be observed. It can be seen that the number and size of precipitates increased with exposure to 1100 °C

(Fig. 12b and c) in such a way that after 1000 h many particles reached more than 10 μm in length. According to the EDXS compositional map presented in Fig. 13, the precipitates were mainly Mo-enriched.

4. Conclusions

A TBC system was thoroughly characterized after exposure to a high temperature. The top coat, Y_2O_3-stabilized ZrO_2, was initially composed of a mixture of tetragonal and cubic phases. Exposure to 1100 °C for 600 h reduced the stability of the tetragonal phase and a fraction of the monoclinic phase was formed during cooling. After 600 h, the amount of the monoclinic phase increased with exposure time, reaching 23.4 wt% in samples exposed for 1700 h. The TGO was essentially composed of Al_2O_3. However, after 800 h of exposition to 1100 °C complex, highly porous (Ni, Cr)-enriched oxides were formed. These oxides are expected to reduce the fatigue strength of the coatings due to their effect on crack generation and propagation. After 600 h, the TGO reached a thickness of 5 μm, which is considered critical for catastrophic failure of the TBC system. Nevertheless, no delamination was observed at any point during the tests, even though the TGO thickness after 1700 h was 6.7 μm. The microstructure of the Inconel 625 substrate after exposure to a high temperature was composed of austenite and a large amount of Mo-rich precipitates.

Acknowledgments

This work was supported by COLCIENCIAS and Empresas Públicas de Medellín (EPM) through the co-funded Project no. 111845421942. The authors are grateful to the Materials Characterization Laboratory at the National University of Colombia in Medellín for providing the characterization instruments.

References

[1] F. Cernuschi, P. Bianchi, M. Leoni, P. Scardi, Thermal diffusivity/microstructure relationship in Y-PSZ thermal barrier coatings, Journal of Thermal Spray Technology 8 (1) (1999) 102–109.
[2] J.D. Osorio, A. Toro, and J.P. Hernández-Ortiz, Thermal barrier coatings for gas turbine applications: failure mechanisms and key microstructural features, Dyna 79 (176) (2012) 149–58.
[3] H.X. Deng, H.J. Shi, H.C. Yu, B. Zhong, Effect of heat treatment at 900 °C on microstructural and mechanical properties of thermal barrier coatings, Surface and Coatings Technology 205 (2011) 3621–3630.
[4] N.P. Padture, M. Gell, E.H. Jordan, Thermal barrier coatings for gas-turbine engine applications, Science 296 (2002) 280–284.
[5] R.W. Trice, Y.J. Su, J.R. Mawdsley, K.T. Faber, Effect of heat treatment on phase stability, microstructure, and thermal conductivity of plasma-sprayed YSZ, Journal of Materials Science 37 (2002) 2359–2365.
[6] R.L. Jones, R.F. Reidy, D. Mess, Scandia, yttria-stabilized zirconia for thermal barrier coatings, Surface and Coatings Technology 82 (1996) 70–76.
[7] P.M. Boyce, Gas Turbine Engineering Handbook, Second ed., Gulf Professional Publishing, Houston, Texas, USA, 2002.
[8] M.R. Winter, D.R. Clarke, Oxide materials with low thermal conductivity, Journal of the American Ceramic Society 90 (2007) 533–540.
[9] X. Song, M. Xie, F. Zhou, G. Jia, X. Hao, S. An, High-temperature thermal properties of yttria fully stabilized zirconia ceramics, Journal of Rare Earths 29 (2) (2011) 155–159.
[10] J.D. Ballard, J. Davenport, C. Lewis, W. Nelson, R.H. Doremus, L.S. Schadler, Phase stability of thermal barrier coatings made from 8 wt% yttria stabilized zirconia: a technical note, Journal of Thermal Spray Technology 12 (1) (2003) 34–37.
[11] D. Zhu, R.A. Miller, Sintering and creep behavior of plasma-sprayed zirconia- and hafnia based thermal barrier coatings, Surface and Coatings Technology 108–109 (1998) 114–120.
[12] V. Lughi, D.R. Clarke, High temperature aging of YSZ coatings and subsequent transformation at low temperature, Surface and Coatings Technology 200 (2005) 1287–1291.
[13] M.D. Chambers, D.R. Clarke, Effect of long term, high temperature aging on luminescence from Eu-doped YSZ thermal barrier coatings, Surface and Coatings Technology 201 (2006) 3942–3946.
[14] S. Deshpande, A. Kulkarni, S. Sampath, H. Herman, Application of image analysis for characterization of porosity in thermal spray coatings and correlation with small angle neutron scattering, Surface and Coatings Technology 187 (2004) 6–16.
[15] A. Portinha, V. Teixeira, J. Carneiro, J. Martins, M.F. Costa, R. Vassen, D. Stoever, Characterization of thermal barrier coatings with a gradient in porosity, Surface and Coatings Technology 195 (2005) 245–251.
[16] A. Feuerstein, J. Knapp, T. Taylor, A. Ashary, A. Bolcavage, N. Hitchman, Technical and economical aspectsof current thermal barrier coating systemsfor gas turbine engines by thermal spray and EBPVD: a review, Journal of Thermal Spray Technology 17 (2) (2008) 199–213.
[17] A.R. Nicoll, G. Wahl, The effect of alloying additions on M–Cr–Al–Y systems: an experimental study, Thin Solid Films 95 (1982) 21–34.
[18] C.S. Richard, G. Béanger, J. Lu, J.F. Flavenot, The Influences of heat treatments and interdiffusion on the adhesion of plasma-sprayed NiCrAlY coatings, Surface and Coatings Technology 82 (1996) 99–109.
[19] J.G. Smeggil, Some comments on the role of yttrium in protective oxide scale adherence, Materials Science and Engineering: A 87 (1987) 261–265.
[20] A.G. Evans, D.R. Mumm, J.W. Hutchinson, G.E. Meier, F.S. Pettit, Mechanisms controlling the durability of thermal barrier coatings, Progress in Materials Science 46 (2001) 505–553.
[21] J.A. Nychka, T. Xu, D.R. Clarke, A.G. Evans, The stresses and distortions caused by formation of a thermally grown alumina: comparison between measurements and simulations, Acta Materialia 52 (2004) 2561–2568.
[22] M. Martena, D. Botto, P. Fino, S. Sabbadini, M.M. Gola, C. Badini, Modelling of TBC system failure: stress distribution as a function of TGO thickness and thermal expansion mismatch, Engineering Failure Analysis 13 (2006) 409–426.
[23] P. Niranatlumpong, C.B. Ponton, H.E. Evans, The failure of protective oxides on plasma-sprayed NiCrAlY overlay coatings, Oxidation of Metals 53 (3–4) (2000) 241–258.
[24] A. Rico, J. Gómez-García, C.J. Múnez, P. Poza, V. Utrilla, Mechanical properties of thermal barrier coatings after isothermal oxidation. Depth sensing indentation analysis, Surface and Coatings Technology 203 (2009) 2307–2314.
[25] D.R. Clarke, C.G. Levi, Materials design for the next generation thermal barrier coatings, Annual Review of Materials Research 33 (2003) 383–417.
[26] I. Spitsberg, K. More, Effect of thermally grown oxide (TGO) microstructure on the durability of TBCs with PtNiAl diffusion bond coats, Materials Science and Engineering: A 417 (1–2) (2006) 322–333.
[27] X. Chen, M.Y. He, I. Spitsberg, N.A. Fleck, J.W. Hutchinson, A. G. Evans, Mechanisms governing the high temperature erosion of thermal barrier coatings, Wear 256 (2004) 735–746.
[28] L. Hu, D.B. Hovis, A.H. Heuer, Transient oxidation of a C–Ni–28Cr–11Al alloy, Oxidation of Metals 73 (1) (2010) 275–288.
[29] A. Reddy, D.B. Hovis, A.H. Heuer, A.P. Paulikas, B.W. Veal, In situ study of oxidation-induced growth strains in a model NiCrAlY bond-coat alloy, Oxidation of Metals 67 (3–4) (2007) 153–177.
[30] J.R. Davis, Heat Resistant Materials (ASM Specialty Handbook), ASM International, Materials Park, Ohio, USA, 1997.
[31] S.K. Rai, A. Kumar, V. Shankar, T. Jayakumar, K.B.S. Rao, B. Raj, Characterization of microstructures in Inconel 625 using X-ray diffraction

peak broadening and lattice parameter measurements, Scripta Materialia 51 (1) (2004) 59–63.
[32] R.C. Reed, in: The Superalloys: Fundamentals and Applications, Cambridge University Press, New York, USA, 2006.
[33] J.C. Zhao, M. Larsen, V. Ravikumar, Phase Precipitation and time–temperature-transformation diagram of hastelloy X, Materials Science and Engineering: A 293 (2000) 112–119.
[34] T.H. Lee, S.J. Kim, Y.C. Jung, Crystallographic Details of precipitates in Fe–22Cr–21Ni–6Mo–(N) superaustenitic stainless steels aged at 900 °C, Metallurgical and Materials Transactions A 31A (2000) 1713–1723.
[35] J. Goldstein, D.E. Newbury, D.C. Joy, C.E. Lyman, P. Echlin, E. Lifshin, L. Sawyer, J.R. Michael, Scanning Electron Microscopy and X-ray Microanalysis, Third ed., Springer, New York, USA, 2003.
[36] P. Liao, T. Chen, P. Chung, A. Fast, Algorithm for multilevel thresholding, Journal of Information Science and Engineering 17 (2001) 713–727.
[37] X.J. Lu, P. Xiao, Constrained sintering of YSZ/Al_2O_3 composite coating on metal substrates produced from eletrophoretic deposition, Journal of the European Ceramic Society 27 (2007) 2613–2621.
[38] D. Zois, A. Lekatou, M. Vardavoulias, A microstructure and mechanical property investigation on thermally sprayed nanostructured ceramic coatings before and after a sintering treatment, Surface and Coatings Technology 204 (2009) 15–27.
[39] A. Cipitria, I.O. Golosnoy, T.W. Clyne, A sintering model for plasma-sprayed zirconia TBCs. Part I: free-standing coatings, Acta Materialia 57 (2009) 980–992.
[40] B. Siebert, C. Funke, R. Vaben, D. Stobver, Changes in porosity and Young's modulus due to sintering of plasma sprayed thermal barrier coatings, Journal of Materials Processing Technology 92–93 (1999) 217–223.
[41] D.R. Clarke, Materials selection guidelines for low thermal conductivity thermal barrier coatings, Surface and Coatings Technology 163–164 (2003) 67–74.
[42] J. Ilavsky, J.K. Stalick, J. Wallace, Thermal spray yttria-stabilized zirconia phase changes during annealing, Journal of Thermal Spray Technology 10 (3) (2001) 497–501.
[43] N. Yoshikawa, A. Kikuchi, S. Taniguchi, Tetragonal to monoclinic transformation in YTZP joined with metallic materials, Journal of Materials Science 34 (1999) 5885–5891.
[44] H.G. Scott, Phase relationships in the zirconia–yttria system, Journal of Materials Science 10 (1975) 1527–1535.
[45] J. Ilavsky, J.K. Stalick, Phase composition and its changes during annealing of plasma-sprayed YSZ, Surface and Coatings Technology 127 (2–3) (2000) 120–129.
[46] G.D. Girolamo, C. Blasi, L. Pagnotta, M. Schioppa, Phase evolution and thermophysical properties of plasma sprayed thick zirconia coatings after annealing, Ceramics International 36 (2010) 2273–2280.
[47] D.R. Clarke, R.J. Christense, V. Tolpygo, The evolution of oxidation stresses in zirconia thermal barrier coated superalloy leading to spalling failure, Surface and Coatings Technology 94–95 (1997) 89–93.
[48] A.M. Karlsson, J.W. Hutchinson, A.G. Evans, A fundamental model of cyclic instabilities in thermal barrier systems, Journal of the Mechanics and Physics of Solids 50 (2002) 1565–1589.
[49] I. Spitsberg, D.R. Mumm, A.G. Evans, On the failure mechanisms of thermal barrier coatings with diffusion aluminide bond coatings, Materials Science and Engineering: A 394 (2005) 176–191.
[50] V.K. Tolpygo, D.R. Clarke, Surface rumpling of a (Ni, Pt) Al bond coat induced by cyclic oxidation, Acta Materialia 48 (2000) 3283–3293.
[51] Y.H. Sohn, J.H. Kim, H.E. Jordan, M. Gell, Thermal cycling of EB-PVD/MCrAlY thermal barrier coatings: I. Microstructural development and spallation mechanisms, Surface and Coatings Technology 146-147 (2001) 70–78.
[52] V.K. Tolpygo, D.R. Clarke, Rumpling of CVD (Ni,Pt)Al diffusion coatings under intermediate temperature cycling, Surface and Coatings Technology 203 (2009) 3278–3285.
[53] W.R. Chen, X. Wu, B.R. Marple, R.S. Lima, P.C. Patnaik, Pre-oxidation and TGO growth behaviour of an air-plasma-sprayed thermal barrier coating, Surface and Coatings Technology 202 (2008) 3787–3796.
[54] H. Hindam, D.P. Whittle, Microstructure, adhesion and growth kinetics of protective scales on metals and alloys, Oxidation of Metals 18 (5–6) (1982) 245–284.
[55] T.J. Nijdam, L.P.H. Jeurgens, W.G. Sloof, Promoting exclusive α-Al_2O_3 growth upon high-temperature oxidation of NiCrAl alloys: experiment versus model predictions, Acta Materialia 53 (2005) 1643–1653.